Direct observation of strong coupling in a dense plasma

D. Riley,* I. Weaver, and D. McSherry
School of Mathematics and Physics, The Queen's University of Belfast, University Road, Belfast BT7 1NN, United Kingdom

M. Dunne
AWE plc, Reading RG7 4PR, Berkshire, United Kingdom

D. Neely and M. Notley
Rutherford-Appleton Laboratory, Chilton, Didcot, Oxon OX11 OQX, United Kingdom

E. Nardi
Department of Particle Physics, Weizmann Institute of Science, 11-76100 Rehovot, Israel
(Received 17 May 2001; published 14 October 2002)

We present differential x-ray scattering cross sections for a radiatively heated plasma showing overall consistency, in both form and absolute value, with theoretical simulations. In particular, the evolution of the plasma from a strongly coupled high density phase to a lower density weakly coupled phase is quite clearly shown in both experiment and simulation. The success of this experiment shows that x-ray scattering has the potential to become an extremely useful diagnostic technique for dense plasma physics.

DOI: 10.1103/PhysRevE.66.046408 PACS number(s): 52.70.La

I. INTRODUCTION

The properties of dense plasmas are of wide interest, for example, to researchers in inertial confinement fusion, laser ablation, stellar structure, as well as planetary physics [1,2]. An important phenomenon in such plasmas is *strong coupling* [3]. This occurs when the Coulomb interaction energy between the pairs of charged particles is greater than their thermal kinetic energy and leads to short range order, as in a liquid metal. This phenomenon is expected to have a significant effect on many plasma properties such as thermal and electrical conductivity. We describe, here, experiments in which strong coupling between the ions of a plasma is observed in a direct way via measurements of the x-ray scattering cross sections. The measured cross sections are broadly consistent with the theoretical simulations. Despite the smearing effects of density and temperature gradients in the plasma, we have been able to observe the transition from a dense strongly coupled plasma to a low density weakly coupled plasma. This success points to the possibility of developing the technique of x-ray scattering into a powerful new diagnostic of dense plasmas.

The strong coupling parameter for ions in a plasma was introduced by Brush, Sahlin, and Teller [4], and is given by

$$\Gamma = \frac{(Z^*e)^2}{R_i k T_i}, \tag{1}$$

where Z^*e is the average ionic charge, R_i is the average interionic separation, and kT_i is the average ion temperature. For laser plasmas, this parameter is commonly above unity for at least part of the plasma. In order to investigate this phenomenon with x-ray scattering methods, we have used volumetric radiative heating of a thin foil in an attempt to reduce the plasma gradients, while retaining the condition $\Gamma > 1$ early in the heating pulse. In the following section, we outline the key features of the experimental technique. In Sec. III, we discuss the hydrodynamic simulations that are inevitably an important part of experimental dense plasma physics, and finally in Sec. IV we present results discussion.

II. EXPERIMENTAL ARRANGEMENT

The experiments were carried out at the VULCAN laser facility of the Rutherford-Appleton Laboratory. Figure 1 shows a schematic of the experiment. A brief outline is as follows. The main heating beams were approximately Gaussian in shape with 800-ps full width at half maximum duration, after frequency doubling to 532-nm wavelength. Six beams were used to irradiate the Au foils (three each side). Each beam delivered ~70 J onto target. Focusing with phased-zone plates (PZP) [5] gave a smooth flat topped profile of 1.5 mm diameter, resulting in an irradiance of $\sim 10^{13}$ W cm^{-2}. The gold foils were 1500 Å thick with a 0.5-μm layer of CH supporting them on the side facing away from the lasers. The x-ray emission from this type of foil has been well characterized by others [6–8] and has a broad smooth spectral structure. For our case, the flux through the rear of the Au is estimated to be ~20% of the incident laser intensity [8] giving an equivalent black body temperature of ~66 eV. The Au foils were placed facing each other 8 mm apart. The experiments were related to earlier work [9] with single-sided irradiation that was, however, less conclusive due to much poorer temporal resolution and severe temperature and density gradients.

The sample Al foil was 1 μm thick and coated with 0.2 μm of CH on each side. The CH coating on both the Au heating foils and on the target absorbed much of the longer wavelength soft x rays that would otherwise be absorbed

*Corresponding author. Email address: d.riley@qub.ac.uk

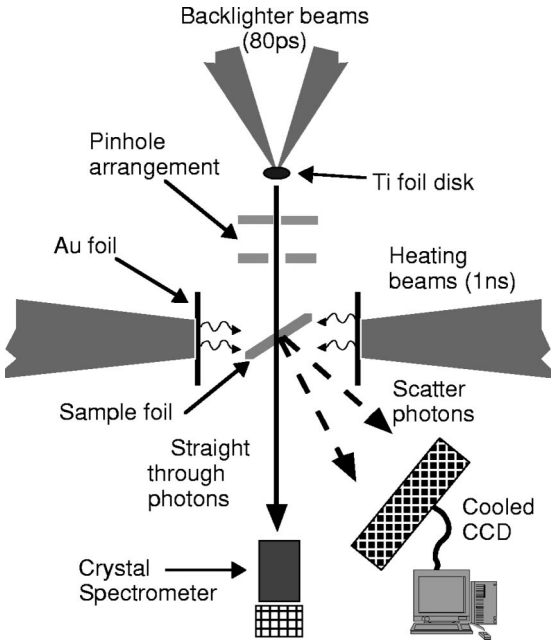

FIG. 1. Schematic of the experiment (not to scale). The timing between the main heating pulses and the backlighter pulses was monitored to ~30 ps. X-ray streak measurements showed that the Ti He-α x-ray pulse duration was 80–100 ps. Extensive test shots showed that the screening shields (not shown) ensured that only photons scattered from the sample foil were collected.

close to the Al surface, leading to stronger temperature gradients. The CH layer on the sample also helped to constrain the expansion of the Al foils and thus reduced the density gradients. The sample foils ($5\times5\,\mathrm{mm}^2$) were stretched across a (shaped mount and placed between the Au foils at 45° to them as in Fig. 1.

A pair of shorter pulse laser beams (80 ps) were synchronized to the longer pulse and used to heat a Ti foil target at intensities of $(1-2)\times10^{15}\,\mathrm{W\,cm}^{-2}$ at 532-nm wavelength. This resulted in a laser plasma that was a strong source of He-like Ti radiation [10] in particular, the $1s^2$-$1s2p$ ^1P (He-α line) and ^3P transitions at ~2.6 Å and the associated Li-like dielectronic satellites. This radiation passed through the pinhole system, of Fig. 1, onto the sample foil in a cone of 6° divergence. The angle of the sample meant that the area probed was an ellipse with axes $2.1\times2.8\,\mathrm{mm}^2$. Most of the He-$\alpha$ line radiation passed through the sample and into a so-called ''straight-through spectrometer'' consisting of a charge coupled device (CCD) coupled to a Si(111) crystal. A typical spectrum is seen in Fig. 2. The small number of scattered x-ray photons were detected with a cooled CCD placed to cover an 18° angular range in the horizontal plane. This so-called ''scatter-CCD'' could be moved on a rail to sample a different range of angles. In fact, two positions were used for this experiment with the highest angle at one position made to overlap with the lowest angle of the other. We estimate the systematic error in the angle to be of order ~1°. The scattering cross sections were calculated by counting the detected photons and comparing them to the number of photons passing through the known thickness of the targets. This latter number was calculated from the brightness of the

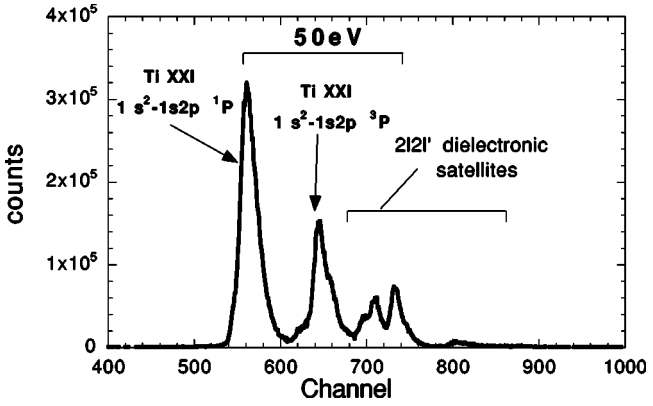

FIG. 2. Example of an averaged line out from the CCD spectrometer used to monitor the incident beam of Ti He-α photons.

''straight-through'' spectrum combined with an estimate of the efficiency of the spectrometer, as outlined below.

The scatter CCD was a 1024×256 pixel EEV-3011OE CCD chip with 26-μm square elements. An absorbed photon at 4.75 keV generates ~1300 electron-hole pairs and the amplifier was sensitive to ~36.5 eV (10 electrons). Thermal, read and shot noise limited the resolution further to ~200 eV. As can be seen in Fig. 2, the group of lines around the Ti He-α group spans only ~50 eV in energy and was by far the brightest feature in the kilovolt region and so represented, for our purposes, an effectively monochromatic source. The filtering of 250-μm Be and 25-μm Al with 50-μm Mylar, combined with the modest irradiance of the heating pulses, prevented too many softer x rays from the Au foils from being detected by the scatter CCD. Since the number of scattered photons incident on the scatter CCD was low ($\sim3\times10^3$), the chances of multiple hits in a single pixel was low. In fact, with the $\leqslant$1 keV radiation from Au being suppressed, >90% of pixels were empty even after accounting for split events, and we were able to make histograms of the pixels for each data shot and count how many photons in the He-α group were detected in single pixel events. The likelihood of single pixel detection (as opposed to split events where the electron cloud, generated by a photon, is split between pixels) was calibrated at 5.9 keV using an ^{55}Fe radioactive source. Kraft *et al.* [11] have shown that we can then scale this result, using their ''slab'' model, giving a single pixel detection efficiency of 0.27 ± 0.02 at 4.75 keV. The data were taken for angles up to 40°, higher angles were not practicable due to the position of the Au heater foils. It should be noted that null shots were taken with the sample mount, but no sample foil present which showed that, at worst, less than 3% of photons (typically <1%) came from stray scatter other than from the sample.

The Si(111) crystal used to monitor the flux of probing photons incident on the sample was also calibrated with the same ^{55}Fe radioactive source. This was done by setting up the ''straight-through'' CCD with the Si crystal as a spectrometer with the ^{55}Fe source as the emission source. The CCD was cooled to $-24\,^{\circ}\mathrm{C}$ and was integrated for 1 min. This was repeated 50 times and the histograms from each run added together. This data was analyzed and combined with

the single pixel efficiency of the CCD, already determined as described above, allowing us to estimate the integrated reflectivity as being half way between that predicted for a mosaic crystal and for a single crystal [12]. Scaling this to 4.75 keV is more problematic than for the single pixel efficiency of the CCD as the crystal properties may vary with penetration depth, however, we have assumed that it is also half way for this photon energy and use a value of 0.09 mrad for integrated reflectivity. The systematic errors in the overall calibration due to errors in measuring CCD quantum efficiency, statistical error in calibration histogram, ^{55}Fe source calibration, and crystal calibration are estimated to be ~30%.

III. HYDRODYNAMIC SIMULATION

The experimental arrangement is not well suited to independent plasma diagnostic, at least not on a shot-to-shot basis. Furthermore, diagnostics of this type of high density low temperature plasma are not trivial to implement or interpret because the density is too high for optical interferometry and the spectral emission is expected to be optically thick. Therefore, we have, in common with many others, used simulation as a guide to the plasma conditions.

Apart from the plasma conditions themselves, the main issue is uniformity. There is likely to be nonuniformity from two sources. First, the geometry of the experiment means that the different parts of the sample may receive different incident fluxes despite the symmetry of the setup. Second, the aluminum foil has to have a reasonable thickness compared to the tamping layer so that scatter is dominated by the Al plasma. This means that despite using x-ray heating, there will be some axial gradients normal to the plane of the sample foil.

Dealing with the first issue, in the absence of a radiation hydrodynamics code that can deal fully with this relatively complex geometry, we have developed a simple numerical model of the incident flux that takes a flat topped black body source with 1.5 mm diameter to represent the emission through the Au foils, with the PZP phase plates. A Lambertian emission law is then used to ray trace from each element of the source to each areal element of the sample foil to give the incident flux from one side and from the combined effect of two Au foils. Figure 3 shows the results of such calculations. The contour map shows that in the probed region (dashed line), the total incident flux is uniform to around 20%.

In modeling the plasma for comparison with experiment, we have taken data from a simulation using the two-dimensional NYM radiation-hydrodynamics code [13,14]. In this simulation, the emission from the gold foil is calculated from a nonlocal thermodynamic equilibrium model for the pulse duration, the intensity, and the wavelength used. We note here that this code predicted a radiation temperature of 65 eV at the rear of the Au foils and ~21-eV flux temperature coming into the sample foil. These values are consistent with the experimental x-ray conversion efficiency [8] and with our subsequent determination of flux onto the foil in Fig. 3. The geometry of our experiment meant that the expansion was expected to be largely one dimensional and this was confirmed by the simulation. A line out through the center of the simulated foils was taken to represent the conditions probed by the experiment. The results of the simulation are shown in Fig. 4. The NYM code uses a fixed boundary to simulate double-sided irradiance and so the graphs show data for one-half of the foil only. Despite using a thin foil, the gradients present are still quite large and so, for the calculation of theoretical cross sections, the simulated sample foil was divided into three parts of equal mass and the average conditions for each third part is used to generate a cross section, the three being then averaged for each probe time. Division into three was chosen since the calculations of the cross sections would be extremely time consuming to perform for each cell of the radiation-hydrodynamics code, and the variation in cross section with plasma conditions is not so fast as to warrant such detailed treatment. Furthermore, the uncertainties of simulation coupled with the modest error bars of the data mean that only a limited amount would be gained from individual cell calculations. At each time in Fig. 4, the approximate values of Γ for the averaged thirds are indicated, calculated using the Z^* derived from the inferno average atom model [15].

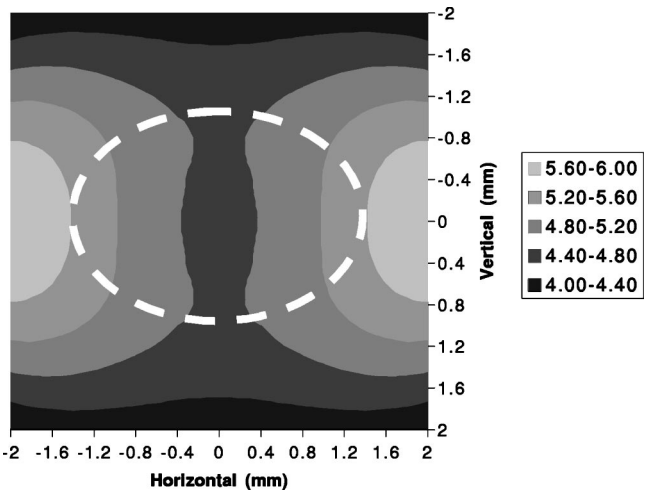

FIG. 3. Contour map of a section of the sample plane showing the total intensity of x-ray heating in units of 10^{10} W cm^{-2}. The dashed curve is the imprint of the backlighter cone of Ti He-α x rays.

In Fig. 5, we show the calculated cross section for individual thirds of the foil at the earliest time ($t = +0.5$ ns). The cross sections of the two innermost parts of the plasma are similar, indicating a strongly coupled plasma that leads to a pronounced peak in the cross section. The outer third is a lower density weakly coupled plasma and the cross section is thus monotonically decreasing, as expected for independent scatterers and simply reflects the atomic form factor for the ions. It is clear that the effect of the outer layer is to make the peak due to the strongly coupled regions much less obvious. Nevertheless, the averaged cross section has a flattened appearance in contrast to the more steeply sloping weakly coupled case.

IV. RESULTS

Figure 6 shows the experimentally determined cross sections. We have taken five overlapping data points per shot by

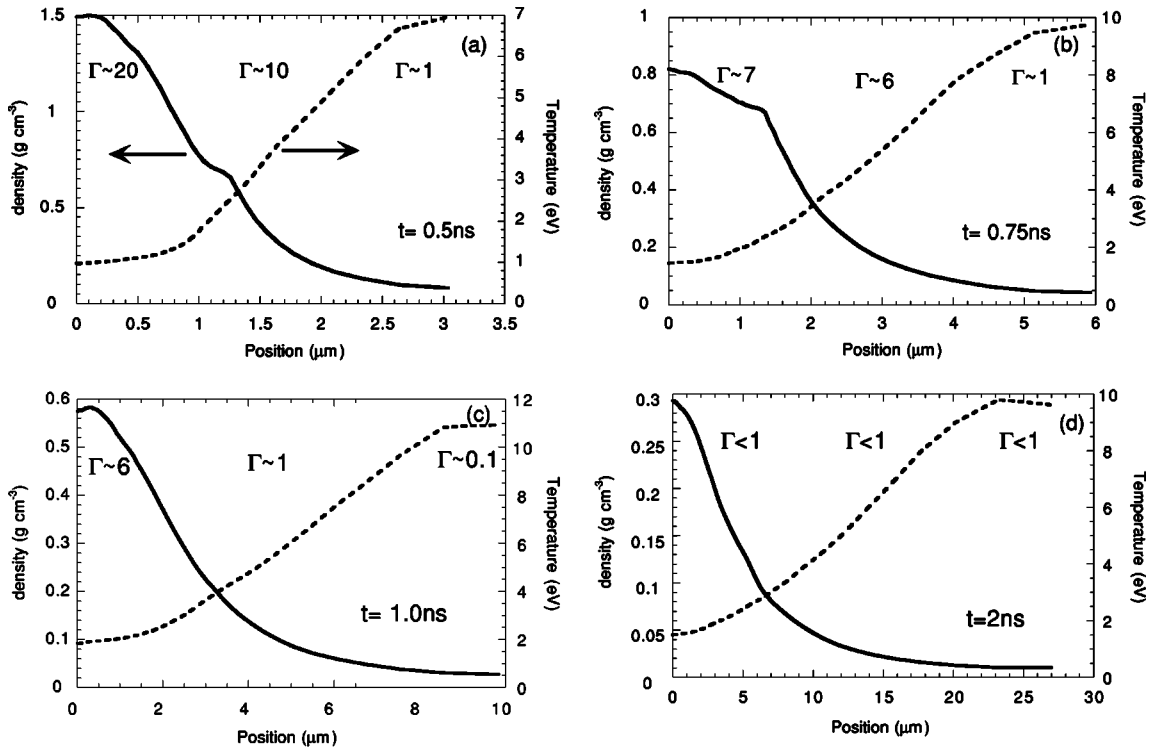

FIG. 4. Hydrodynamic simulation of the sample at various delays relative to the peak of the heating beams. Only one-half of the target is shown, since the code uses the symmetry of the experiment as a boundary condition. Only the conditions for the Al are shown, the CH is hotter and is calculated to contribute only ~5% of scatter signal due to its lower number of bound electrons. The values of Γ are those for the averaged conditions in each third of the mass of the foil.

integrating over one-third of the CCD for each point (equivalent 6° resolution in the horizontal plane) and shifting the center of measurement by one-sixth of a CCD screen for the next point. The error bars are essentially given by $N^{1/2}$, where N is the total number of photons detected for a particular data point. Since some points are averages of two or three shots whilst others are based on single shots, there is a variation in the size of the error bars. We can see that there is an evolution from the flattened cross section at 0.5-ns delay towards a more steeply sloping cross section at 2-ns delay.

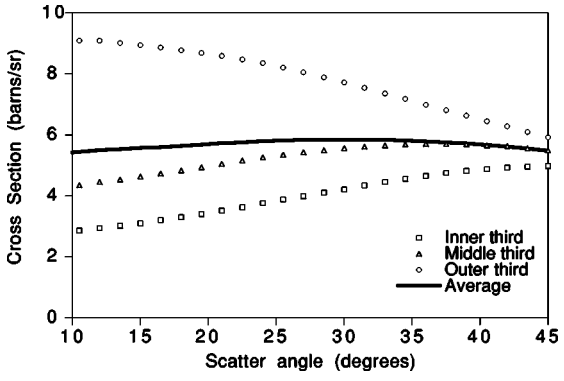

FIG. 5. Scattering cross sections calculated for the averaged conditions in each third of the sample at 0.5 ns after the peak of the heating pulse. As can be seen, the distinctive suppression of cross section at low angle is to some degree hidden by the effect of the low density outer part of the sample.

This progression is as expected since, at late time, the plasma is expected to be at lower density and to be fairly weakly coupled. In this case, the atomic form factor for individual ions will dominate, resulting in the steeper ''fall off'' with angle. On the other hand, at 0.5-ns delay, the plasma is expected still to be mostly at higher density and strongly coupled, in which case the collective scattering structure factor for the plasma will be more important and will suppress scatter at lower angles.

In Fig. 6, the solid lines represent simulation of the expected, temperature and density averaged cross section, using the hydrodynamic data of Fig. 4 with the inferno model combined with a hypernetted chain model for ion-ion correlation [16,17]. The dashed lines represent the same calculations except this time with the activity expansion (ACTEX) [18] ionization model used to determine Z^*. In Fig. 6(a), we can see that, for early time, the flattened cross section of the data is quite well produced by the inferno simulation with about a 20% difference in absolute value. In Fig. 6(b), the error bars are larger as fewer shots are taken. The general trend is again flat, as predicted by simulation, although the difference in the absolute values between the inferno simulation and the experiment is ~40%. Skipping for the moment to Fig. 6(d), we can see that the absolute values are in quite good agreement and the shape is reasonably well reproduced. At this time, we expect a weakly coupled plasma with a monotonically decreasing cross section that reflects the atomic (or ionic in this case) form factor and this is more or less what is seen.

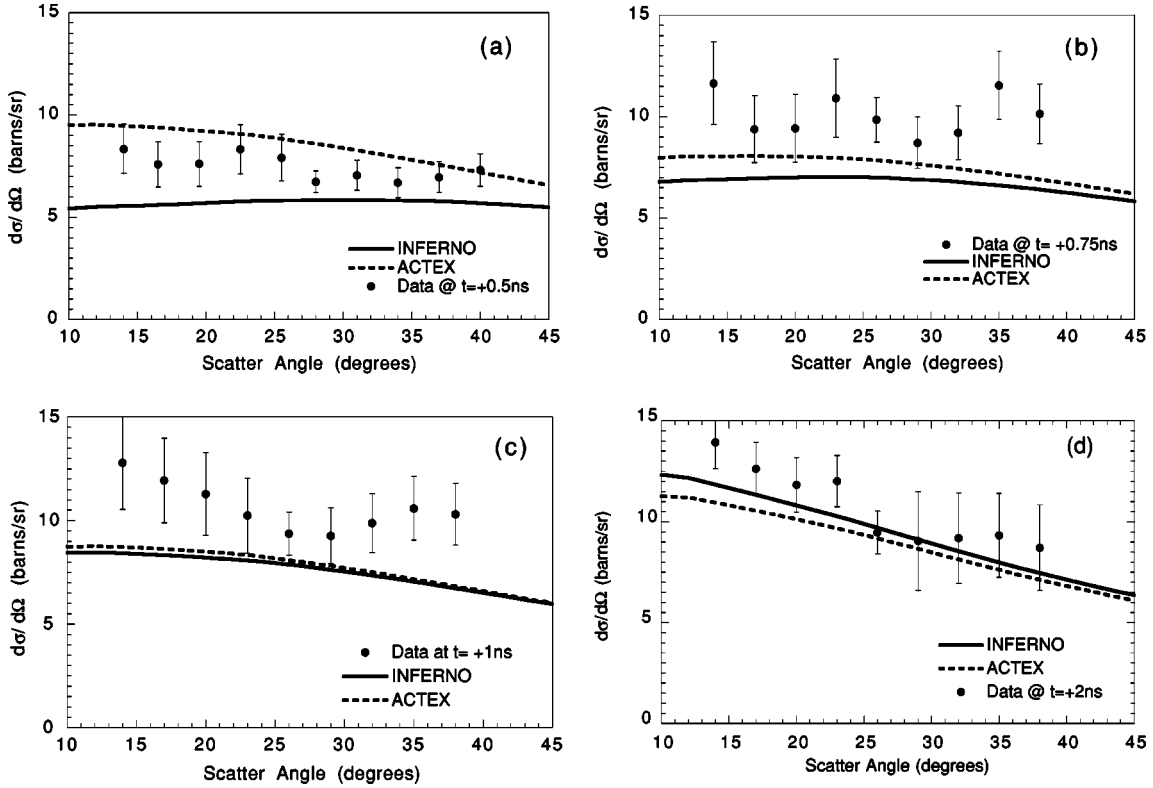

FIG. 6. Experimental x-ray scatter cross sections at the four times in Fig. 4. The two CCD positions were chosen to have one angle in common (to within 1°). The curves are simulated cross sections for the whole sample foil, calculated as described in the text.

Returning to Fig. 6(c), there is less agreement between simulation and experiment. As for Fig. 6(b), there is about 40% absolute value offset between experiment and INFERNO-based simulation, but this time the shape is not well reproduced by either model. The interpretation of the experimental data on its own could suggest that the scattering comes from two distinct regions of plasma: with a weakly coupled part responsible for the lower angle cross section that resembles Fig. 6(d), and a more strongly coupled plasma that gives a cross section that is suppressed at low angles but accounts for the rising curve at higher angle. The superposition of these might then provide the ''dip'' seen in the data. Given that both the INFERNO and ACTEX [18] ionization models were developed for higher density cases, it is possible that whilst both fail to match the data of Fig. 6(c) a different model may be more successful. For the two early times in Fig. 6, there are noticeable differences in the cross section predicted by the two ionization models. One point worth mentioning is that the INFERNO model is able to account for resonance scattering states. Our modeling treats the broad *p*-resonance electrons, present under these conditions, as free electrons for the purposes of calculating ion-ion coupling. If we treat them as bound electrons, we find that the predicted scatter cross section for all times is similar to the weak coupling case shown in Fig. 6(d). This is clearly not the case experimentally.

The comparison of the relative success of the two ionization models needs to be based on the shape of the cross section since the systematic error due to calibration is too large for us to rely on the absolute magnitude. We can compare how well each model fits the data, in a simple way, by using a least squares fit. This was done by assuming that there is some scale factor R, by which we need to multiply the data points of Figs. 6(a) and 6(b) to obtain the ''correct'' calibration. Thus, the sum of squares for N data points is given by

$$S=\frac{1}{N}\sum_{i=1}^{N}\frac{(R\sigma^{i}_{\mathrm{expt}}-\sigma^{i}_{\mathrm{sim}})^{2}}{(\sigma^{i}_{\mathrm{sim}})^{2}}. \tag{2}$$

The parameter R is varied to minimize S, which gives a measure of how well the shape of the cross section fits between experiment and simulation. We have only used the first two times since the models are really only designed for higher densities and it is at higher density that the resonance electrons, which represent an important difference between the models, are present. The scaling is done for both probe times in the same calculation, since any systematic error in calibration should be the same for all data shots. For INFERNO the best fit gives a scale factor $R=0.71$ with $S=0.013$; for ACTEX, $R=0.88$ and $S=0.052$. We should note here that in fact if we just take data from Figs. 6(a), and 6(b) separately, we get a better fit to ACTEX in Fig. 6(a). However, the scale factor R needed is $\sim$55% different from the scale factor needed to get a best fit to the data of Fig. 6(b)—contrary to the likelihood where we have a constant systematic calibration error. On the other hand, treating Fig. 6(a) and 6(b) separately for the INFERNO model leads to scale factors only $\sim$13% different—within the span of typi-

cal statistical error bars. We can also point out that although we have not used the later two times, the ''scale factor'' determined for the first two times, to give a best fit, would still lead to reasonable fits for the later times using the INFERNO model.

V. DISCUSSION AND CONCLUSIONS

From the analysis above, overall it seems that ACTEX does not fit as well as INFERNO to the higher density data. However, the error bars on the data and the nonuniformity of the plasma means that we cannot rush to any firm conclusions. Better uniformity plasma generation and closer bounds on the systematic error in calibration are needed for further progress. Improvements to the plasma uniformity are not easy to make but should be possible. One major problem is that any tamping layer used to confine the sample will contribute to the scatter signal. Possibly, the use of thinner layers with higher Z will be one way forward. The extra bound electrons will help the sample layer dominate over low Z tamping layers.

What the data does show is clear direct experimental evidence of the evolution of the plasma from strong coupling at early times and a weakly coupled plasma at later times. With the exception of data at one probe time the shape of the cross section is reasonably well matched by the simulation. Given the traditional difficulty in obtaining precise absolute values of most parameters in plasma physics, the absolute values of cross section match well to the simulation.

The significance of this work is that the broad regime we are able to investigate is intermediate between the well-researched areas of plasmas and liquid metals and is by no means completely understood theoretically. For this type of plasma, standard methods of plasma diagnosis are difficult. As indicated above, optical emission and absorption spectroscopy are hampered by high opacity and broadening of spectral feature. X-ray-absorption spectroscopy is also hampered by the difficulty of distinguishing between low ionization states. For example, in the current case, $K\alpha$ absorption spectroscopy is prevented by the filled L shell of the Al ions [19].

One problem stated earlier in the paper is the difficulty of implementing independent diagnostics to help constrain estimates of density and temperature, for these types of plasma. In the future, the development of Thomson scatter and/or interferometry [20] methods using x-ray lasers and thermal x-ray sources [21] may make it possible to obtain independent data on the foil conditions with which we can compare the sort of data and simulations presented here.

ACKNOWLEDGMENTS

We would like to thank A. McMullan, A. McCloskey, and A. M. McEvoy for contributions to the crystal calibration and the staff of the Central Laser Facility for providing the excellent laser facilities and support. This work was funded by the U.K. Engineering and Physical Sciences Research Council.

[1] D. Alfe, M. J. Gillan, and G. D. Price, Nature (London) **401**, 462 (1999).
[2] T. Guillot, Science **286**, 72 (1999).
[3] S. Ichimaru, Rev. Mod. Phys. **54**, 1017 (1982).
[4] S. Brush, H. Sahlin, and E. Teller, J. Chem. Phys. **45**, 2102 (1966).
[5] R. M. Stevenson *et al.*, Opt. Lett. **19**, 363 (1994).
[6] D. R. Kania *et al.*, Phys. Rev. A **46**, 7853 (1992).
[7] C. A. Back *et al.*, J. Quant. Spectrosc. Radiat. Transf. **51**, 19 (1994).
[8] P. Celliers and K. Eidmann, Phys. Rev. A **41**, 3270 (1990).
[9] D. Riley, N. C. Woolsey, D. McSherry, and E. Nardi, J. Quant. Spectrosc. Radiat. Transf. **65**, 463 (2000).
[10] D. W. Phillion and C. J. Hailey, Phys. Rev. A **34**, 4886 (1986).
[11] R. P. Kraft *et al.*, Nucl. Instrum. Methods Phys. Res. A **366**, 192 (1995).
[12] B. L. Henke, E. M. Gullikson, and J. C. Davis, At. Data Nucl. Data Tables **54**, 181 (1993).
[13] P. C. Thompson and P. D. Roberts, Laser Part. Beams **2**, 13 (1984).
[14] P. C. Thompson, P. D. Roberts, N. J. Freeman, and P. T. G. Flynn, J. Phys. D **14**, 1215 (1981).
[15] D. A. Liberman, Phys. Rev. B **20**, 4981 (1979).
[16] Y. Rosenfeld, Phys. Rev. E **47**, 2676 (1993).
[17] E. Nardi, Z. Zinamon, D. Riley, and N. C. Woolsey, Phys. Rev. E **57**, 4693 (1998).
[18] R. J. Harrach and F. J. Rogers, J. Appl. Phys. **52**, 5592 (1981).
[19] R. M. More, Adv. At. Mol. Phys. **21**, 305 (1985).
[20] J. Svatos, D. Joyeux, D. Phalippou, and F. Polack, Opt. Lett. **18**, 1367 (1993).
[21] O. L. Landen, S. H. Glenzer, M. J. Edwards, R. W. Lee, G. W. Collins, R. C. Cauble, W. W. Hsing, and B. A. Hammel, J. Quant. Spectrosc. Radiat. Transf. **71**, 465 (2001).